Nanoscale



PAPER

View Article Online
View Journal | View Issue



Cite this: Nanoscale, 2024, 16, 2591

Tunable growth of a single high-density ZIF nanoshell on a gold nanoparticle isolated in an optical trap†

Daniel Jackson, a Maitreya Rose and Maria Kamenetska ** **a,b,c

Here, we demonstrate an all-optical method using an optical tweezer to controllably grow high quality zeolitic imidazolate framework (ZIF) nanoshells on the surface of gold nanoparticles (AuNPs) and monitor the growth *via* darkfield spectroscopy. Our single particle approach allows us to localize an individual NP within a microscope slide chamber containing ZIF precursors at the focus of an optical microscope and initiate growth through localized heating without affecting the bulk system. Darkfield spectroscopy is used to characterize changes to the localized surface plasmon resonance (LSPR) of the AuNP resulting from refractive index changes as the ZIF crystal grows on the surface. We show that the procedure can be generalized to grow various types of ZIF crystals, such as ZIF-8, ZIF-11, and a previously undocumented ZIF variety. Utilizing both computational models and experimental methods, we identify the thickness of ZIF layers to be self-limiting to ~50 nm or less, depending on the trapping laser power. Critically, the refractive index of the shells here was found to be above 1.6, indicating the formation of high-density crystals, previously accessible only through slow atomic layer deposition and not through a bulk heating process. The single particle method developed here opens the door for bottom-up controllable growth of custom nanostructures with tunable optical properties.

Received 21st October 2023, Accepted 8th January 2024 DOI: 10.1039/d3nr05316d

rsc.li/nanoscale

Introduction

E-mail: mkamenet@bu.edu

Gold nanoparticle – metal organic framework (AuNP@MOF) hybrid structures have gained popularity in recent years as surface-enhanced Raman spectroscopy (SERS) substrates, ^{1,2} drug delivery particles, ^{3,4} gas sequestration systems, ^{5–7} reaction catalysts, ^{8–11} and low limit of detection (LOD) sensors. ^{12–15} In order to push these technologies forward new high precision techniques for controlled growth and characterization of particle structures, optical properties, and physical properties are required. Many synthetic procedures for zeolitic imidazolate frameworks (ZIFs), a widely studied and highly stable class of MOFs, generally achieve crystal growth by heating a reaction mixture in ovens or water baths. ^{14,16–18} Procedures for encapsulation of gold nanoparticles in ZIF shells, with ZIF-8 as one of the most common, follow similar heating methods and typically result in low density crystals

with a high porosity and a greater quantity of interparticle pores, due to small crystals conglomerating to form larger particles. 1,2,8,19,20

Optical trapping has been demonstrated to be an effective method to isolate and optically characterize nano- and microparticles in a range of solvent environments. In our previous work, we have shown that optical imaging and force signatures of trapped gold nanoparticles can serve as probes of the local chemical environment. Furthermore, gold nanoparticles experience significant heating when in an optical trap (OT) due to absorption of the trapping laser by the nanoparticle.

In this report we demonstrate targeted growth of high-density ZIF crystals on the surface of a single, 80 nm diameter, AuNP driven by the high temperatures generated in an OT. We find that by heating AuNPs directly in our OT, we can controllably, selectively, and reproducibly grow ZIFs on the surface of a single AuNP on the scale of seconds. Growth of the crystal is monitored through spectral measurements of the plasmonic darkfield scattering signal and Raman spectroscopy of a single, optically trapped AuNP during the course of growth. We find that the growth of the ZIF crystals is self-limiting to ~50 nm beyond the gold nanoparticle surface due to the temperature gradient surrounding the trapped nanoparticle, and thinner shells can be grown by adjusting the laser power. Our

^aDepartment of Chemistry, Boston University, Boston, MA 02215, USA.

^bDepartment of Physics, Boston University, Boston, MA 02215, USA

^cDivision of Material Science and Engineering, Boston University, Boston, MA 02215,

[†]Electronic supplementary information (ESI) available. See DOI: https://doi.org/ 10.1039/d3nr05316d

Paper Nanoscale

measurements, and modeling, indicate that the refractive index of the grown ZIF-8 crystals is ~1.7. This corresponds to high-density, low-porosity ZIF shells which are not accessible using bulk synthesis methods. 19,25 Finally, we show that our procedure for selective single ZIF shell growth is general and can be applied to a variety of ZIF structures, including ZIF-8, ¹⁶ ZIF-11,16 a ZIF-95 isomorph,25 and a novel ZIF compound, which are grown with 2-methylimidazole (2-Mim), benzimidazole (Bim), 6-bromobenzimidazole (6-BBim), and 4-tertbutylimidazole (4-TBim) respectively. We also achieved growth with a variety of metallic ions, including Zn²⁺ and Co²⁺, and in several solvents: ethanol, water, and dimethylformamide (DMF). This technique represents a bottom-up growth method for encapsulation of AuNPs with ZIF crystals for which shell thickness can be controlled and monitored during growth. By demonstrating ZIF growth through direct heating of the substrate on the single particle level rather than of the bulk solution, we open the door for controllable engineering and bottom-up assembly of nanoscale objects from molecular building blocks.

Results

We perform experiments using a homebuilt optical tweezer microscope retrofitted with both darkfield (DF) and Raman spectroscopy imaging capabilities.²¹ Fig. 1A shows a schematic of the optical trapping instrument used in these experiments. Trapping in the sample chamber is achieved with a 1064 nm continuous wave (CW) laser, coupled with a white light annular beam as the DF illumination source. Raman measurements are performed using a 532 nm excitation beam coupled into the DF illumination path. Backscattered light from the particle is collected simultaneously in both a camera and spectrometer, allowing real time tracking of changes to particle optical properties. ^{21,26} The trapping laser is used to isolate and manipulate individual AuNPs in the solution. DF illumination enables us to visualize and measure the scattering spectra of the trapped particles. Raman excitation allowed us to chemically fingerprint the material on the surface of the NP. This instrument was discussed in more detail in our previous work.21

Fig. 1B is a schematic of the growth process used to generate ZIF nanoshells on AuNPs (Au@ZIF), adapted from known encapsulation procedures.^{2,8} Prior to measurements, AuNPs are coated in a polyvinylpyrollidone (PVP) polymer for passivation in organic solvents (e.g. ethanol, DMF) and chelation of metal ions to preferentially nucleate the growth of ZIFs on the AuNP surface. 1,2,8,27 PVP enhances affinity of the AuNP for coordination-polymer spheres through interactions between the pyrrolidone rings and the zinc atoms in the ZIF crystal. 28,29 The particle solution is then combined with the chosen ZIF components, such as 2-Mim and zinc nitrate salt (Zn(NO₃)₂), after which it is injected into a sealed microscope chamber and positioned at the focus of the optical trapping microscope objective. We rely on DF spectroscopy and optical trapping force signatures to reliably trap only single AuNPs, approximately 10 µm above the glass coverslip surface inside the chamber.²¹ Once the particle is trapped, the laser power is

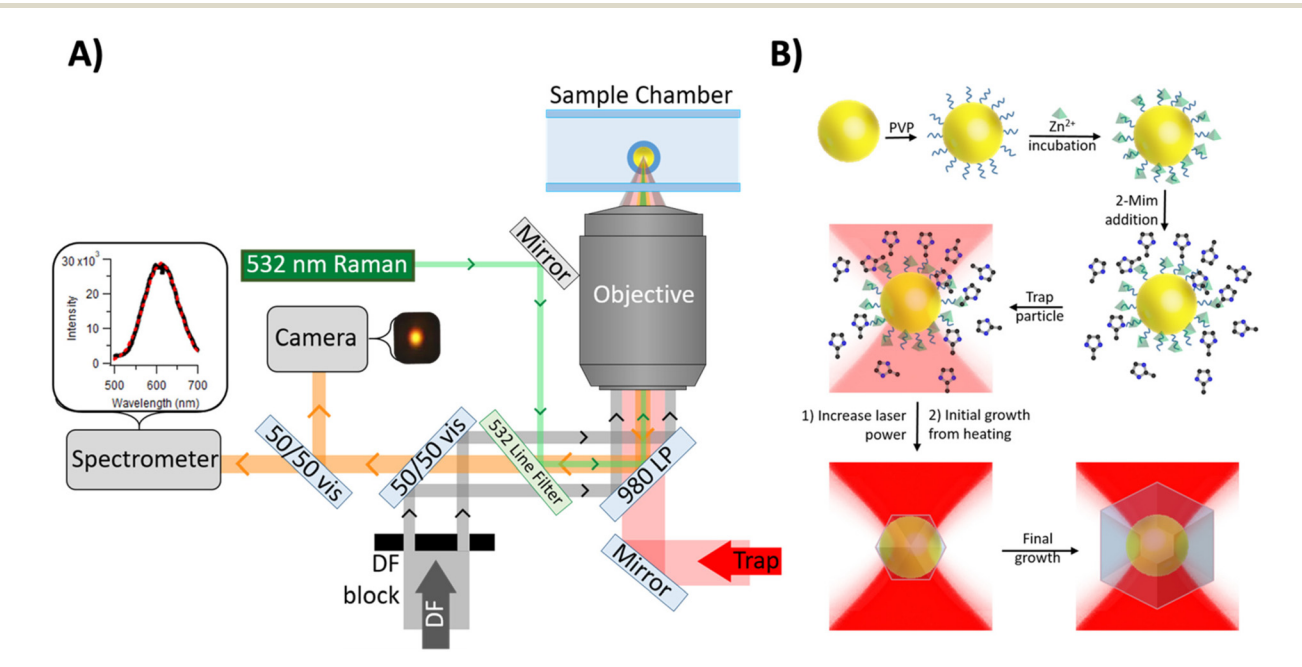


Fig. 1 (A) Schematic of OT built in an inverted microscope configuration, including DF spectroscopy imaging. Red represents our trapping laser. Gray represents the DF illumination (white light). Green is the input Raman excitation laser (532 nm). Orange is the light scattered back by the nanoparticles. At the objective focus is an optically trapped AuNP coated in a ZIF shell. Insets show a representative plasmon scattering spectra and the associated DF images of the particle. Diagram not to scale. (B) Mechanism describing encapsulation of optically trapped AuNPs by ZIF-8 to form single-particle, core@shell structures. PVP = polyvinylpyrollidone, 2-Mim = 2-methylimidazole. Diagram not to scale.

increased to 50 mW or higher, causing the trapped AuNP to heat up as we and others have shown previously. 21,22,24 The

Nanoscale

full experimental procedure is outlined in the ESI.† ZIF-8, which is grown from 2-Mim and Zn(NO₃)₂ as shown

in Fig. 1B, has been extensively characterized and serves as a proof-of-concept for the growth technique presented here. Fig. 2A shows six representative DF spectra of the same optically trapped, 80 nm diameter, AuNP. The spectra are each a 100 ms scan collected at various times within 25 seconds after the onset of heating in the trap. In this case, growth occurs in the presence of ZIF-8 precursors at a concentration of 1 mM 2-Mim and 0.33 mM Zn²⁺. The curves in Fig. 2A are drawn from a larger dataset of spectra collected for each particle during growth at a rate of 10 Hz, with 100 ms acquisition times, shown in the Fig. S1.† The initial spectrum (black) in Fig. 2A, taken immediately after the particle becomes trapped and heated, peaks at 560 nm as measured by a Gaussian fit (dashed lines), which is consistent with expectations for the

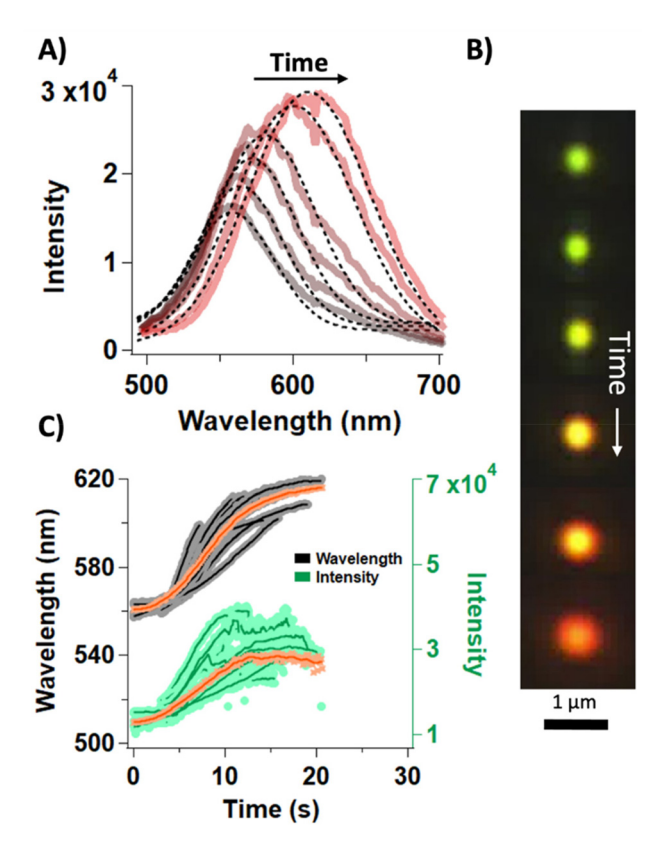


Fig. 2 (A) DF spectra collected following heating of an optically trapped, 80 nm AuNP in ethanol in the presence of ZIF-8 precursors. The gray curve is measured immediately after laser power increase and the red curve is measured 15 seconds later, with a few intermediate spectra also shown. Gaussian fits to the spectra are plotted in dashed black. (B) Camera images corresponding to the spectra in (A). (C) Intensity (green, right axis) and peak wavelength (black, left axis) as extracted from Gaussian fits to the raw spectra plotted against time elapsed since heating onset. Data corresponding to 18 individual AuNPs is plotted here and is representative of the full data set collected in ethanol shown in the ESI.† Data corresponding to curves in (A) is highlighted in orange.

scattering spectra of a bare 80 nm AuNP, indicating no growth prior to measurements. Subsequent spectra peak positions shift towards longer wavelengths and higher amplitudes. Fig. 2B shows camera images captured simultaneously with the six spectra in Fig. 2A, demonstrating the color change. No color change is observed on other particles flowing freely in solution in the same chamber. We also observe a broadening of the spectra in Fig. 1A after the onset of heating, suggesting a deposition of material on the surface which leads to energy transfer from the nanoparticle to the surface layer and a damping of the plasmon response. We attribute variations in spectra to differences in the number, and location, of crystal nucleation sites on the surface of an AuNP, as well as small variations in growth rates resulting in imperfect spheres.

To capture the evolution of DF spectra, we fit the curves in Fig. 2A and S1† with a Gaussian function. In Fig. 2C we plot the peak wavelength (black) and intensity (green) against time elapsed for 18 individual AuNPs trapped and heated at time 0 in the presence of ZIF-8 precursors. The end of the traces marks the point when the particle falls out of the trap. We observe that both wavelength and intensity increase sharply within ~5 seconds of heating onset and approach an asymptote within 25 seconds, indicating no further changes after this time. No similar change of the DF spectra was detected when one or more of the ZIF-8 precursors was missing from the solution, as show in Fig. S2 and S3.† Growth on trapped particles was achieved in a narrow range of concentrations of the precursor materials as shown in Fig. S4.† Once growth on one particle was complete, it was released from the trap and another particle captured to repeat the growth protocol.

Fig. 3 shows a Raman spectrum (black) of a trapped particle, with both the 2-Mim and the Zn precursor present, acquired over one minute after crystal growth was initiated. Peak positions agree well with literature reports for ZIF-8 crystal Raman shifts.7,18 Control experiments performed on optically trapped bare AuNPs (not shown), AuNPs with polymer functionalization (green), AuNPs in the presence of only Zn²⁺ precursor (red), and AuNPs in the presence of only the imidazole precursor (blue), showed no detectable signal as evident in the figure. These results indicate that the observed

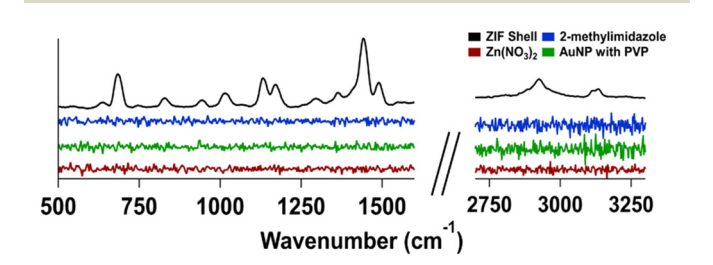


Fig. 3 Raman measurement using a 532 nm excitation beam, with a 1 min acquisition time, performed on a single, optically-trapped, 80 nm AuNP in the presence of PVP polymer (green), 2-Mim (blue), Zn(NO₃)₂ salt (red), and a ZIF-8 crystal grown on the surface (black). A fully labeled ZIF Raman scattering spectra is presented in Fig. S5.†

Raman signal is due to a crystal shell grown at the surface of the AuNP, rather than from free floating precursor molecules.

The red shifting of the DF spectra observed in Fig. 2C for the particle is consistent with encapsulation of nanoparticles with ZIF structures. 1,2 The growth of the crystal around the AuNP replaces the solvent, such as ethanol with a refractive index of n = 1.35 for 1064 nm light, ³⁰ to create an environment with a new refractive index. As a result, the plasmon resonance of the composite particle detected in the far field red shifts relative to a bare AuNP. While all experiments presented in our main figures are performed in ethanol with Zn²⁺ metal ions, we also achieve ZIF-8 growth in water and dimethylformamide (DMF) and find a similar red shifting trend regardless of solvent used (shown in Fig. S6-S8†). Additionally, we demonstrated successful growth of ZIF crystals using Co²⁺ metal ions which also show a redshift (shown in Fig. S9 and S10†). To characterize the density and porosity of the ZIF shells grown here, we model the scattering cross sections of Au@ZIF composite particles in MATLAB using the MNPBEM17 package designed for simulating plasmonic nanoparticle-light interactions.³¹ The model parameters use data from McPeak et al. for the wavelength dependent refractive indices of gold across the visible spectrum, 32 ethanol as the solvent $(n_{560} = 1.36)$, 30 and an adjustable refractive index for the growing ZIF shell. Prior measurements of ZIF-8 crystal refractive indices range from 1.28, to 2.6.1,5,19,33-36 Cookney et al. reports indices ranging from 1.54-1.58 in their high density ZIF-8 crystals, which are grown using a layer by layer growth method.¹⁹ Fig. 4A shows modelled scattering cross sections for an 80 nm AuNP with increasing crystal shell thickness with a refractive index of n = 1.58, following the indices presented by Cookney et al. 19 We observe that a modelled shell thickness of 200 nm or greater produced broad scattering profiles, without a clear resonance peak (Fig. 4A and S11†). This is distinct from our experimental measurements, as shown in in Fig. 2A.

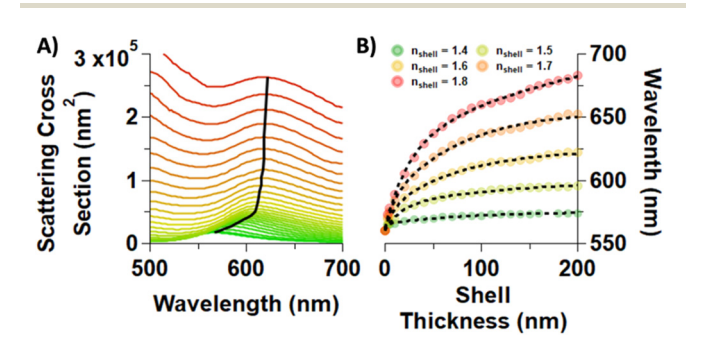


Fig. 4 (A) Modelled scattering cross sections for an 80 nm AuNP in ethanol with a ZIF crystal shell. Each curve has a different shell thickness ranging from 0 nm (greenest curve) to 250 nm (reddest curve) for refractive index n = 1.58. The black line shows the evolution of the resonance peak as the shell thickness varies. Core@shell particles were modeled using MNPBEM17 toolbox in MATLAB.²⁸ (B) The changes in the resonance peak for different ZIF refractive indices and thicknesses. Each point represents the peak location for a given shell thickness and refractive index modelled as in (A). Dashed black lines are a double exponential fit to the data.

Furthermore, our model (Fig. 4A) shows that the magnitude of the calculated scattering cross section, which is proportional to the measured signal intensity, increases monotonically with shell thickness. In contrast, the experimental data in Fig. 2B plateaus after an initial growth period. These results together suggest that shell growth will not reach 200 nm in thickness.

We use our model to estimate the refractive index of the grown ZIF nanoshells. Fig. 4B shows modelled data of the expected peak wavelength for different ZIF shell refractive indices. As expected, the peak red shifts with increasing shell thickness, and then begins to plateau for thicknesses above 100 nm. A double exponential fit line is used to describe the modeled wavelength data. We observe good agreement with

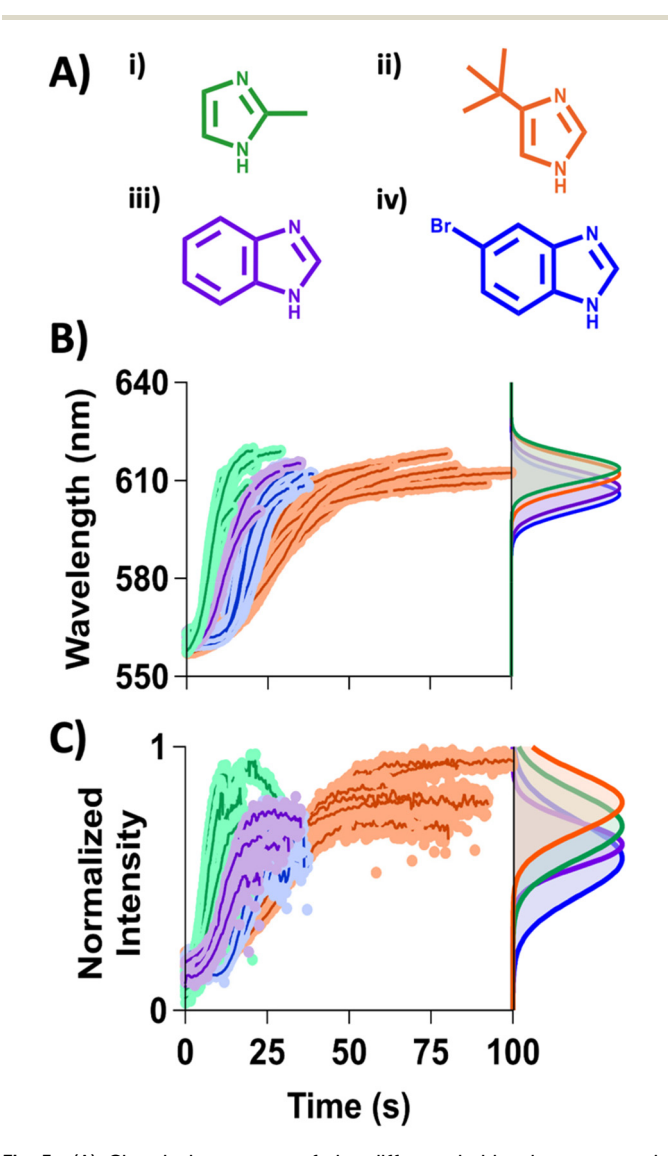


Fig. 5 (A) Chemical structure of the different imidazole compounds used to grow ZIF crystals. (i) 2-Mim, (ii) 4-TBim, (iii) Bim, and (iv) 6-BBim. (B) Plot of the peak wavelength (C) and intensity against time after laser power increase. Color corresponds to the precursor used and are illustrated in (A). On right are Gaussian fits to histograms of the last 3% of the plotted data for each particle. The histograms for both wavelength and intensity are presented in Fig. S12.†

Nanoscale Paper

experimental measurements only with higher index values. It should be noted that for thin shell thickness, small changes to the shell result in large changes in wavelength as shown in Fig. 4B. This illustrates that observed deviations in wavelength would result from very minute changes in the ZIF crystal thickness. Consulting Fig. 2B, we identify n = 1.58, as providing a reasonable fit to our data. These results strongly suggest that the ZIFs grown in our experiments are high density crystals which are distinct from products of bulk-synthesis growth characterized by lower refractive index values of $n \approx 1.4$. ^{19,25}

To demonstrate that this procedure for growing high quality Au@ZIF structures is general and applicable to other ZIF variants, we repeat the single NP ZIF growth procedure illustrated in Fig. 1B in the presence of 2-Mim and three alternative imidazole derivatives, which are shown in Fig. 5A alongside 2-Mim (green): 4-TBim (orange), Bim (purple), and 6-BBim (blue). In Fig. 5B and C we show representative scattering spectra and intensity trajectories, respectively, of a single trapped AuNP recorded in the presence of each molecular precursor and Zn²⁺ at 50 mW of laser power. In all cases, we observe a red shift of the scattering spectra and an increase in intensity followed by the signal plateauing. However, the final asymptote values of wavelength and intensity vary somewhat between the ZIFS. For example, we find that, on average, crystals grown from the substituted imidazole variants 2-Mim, and 4-TBim both reach scattering wavelength of ~615 nm, and the ZIFs grown with the large Bim and the variant 6-BBim reach lower values of ~605 nm. These patterns imply a lower refractive index with larger organic precursors, indicating a lower density crystal, and thus positive correlation between the size of the organic linker and the size of the pores in a MOF.^{5,37}

Our results here are consistent with prior measurements showing that the pore size in ZIF-11 (Bim) is 26% larger than that in ZIF-8 (2-Mim) crystals, as well as having a 19% decrease in metal ion density per unit volume.16

To our knowledge, the ZIF grown with 4-TBim, has not been reported previously.³⁸ Our measurements here are the first to probe its growth dynamics and porosity relative to other ZIFs. In the case of ZIF-8, most particles grow within the first 20 seconds of being exposed to the trapping laser. The more sterically hindered 4-TBim grows slowest, saturating within 75 seconds. The tertbutyl group is a large steric group, and our data suggests that it is reduces the rate of crystal growth, but minimally impacts its optical properties in comparison to 2-Mim. Shells grown using 4-Tbim reach a final wavelength that is similar to that of ZIF-8, although it takes longer to plateau. From these observations, we conclude that the crystal has a similar density to ZIF-8, but a slower growth rate.

The slower growth rate of 4-Tbim offers additional experimental control to examine dynamics and properties of crystal growth with changing laser power. Fig. 6A presents experimental results for growth of 4-Tbim ZIF crystals when held in the optical trap at different trapping laser powers: 30 mW, 40 mW, 50 mW, and 60 mW of trapping laser power. We can see a clear dependence on the trapping laser power of both the rate of growth and the final peak scattering wavelength. For 30 mW of power the average scattering signal shifted by only ~10 nm in 100 seconds, indicating little to no growth. As the power increased, the growth accelerated, and the final saturation wavelength red shifted. At our highest power, 60 mW, we can see that growth saturates within ~10 seconds at a final wavelength of 622 nm.

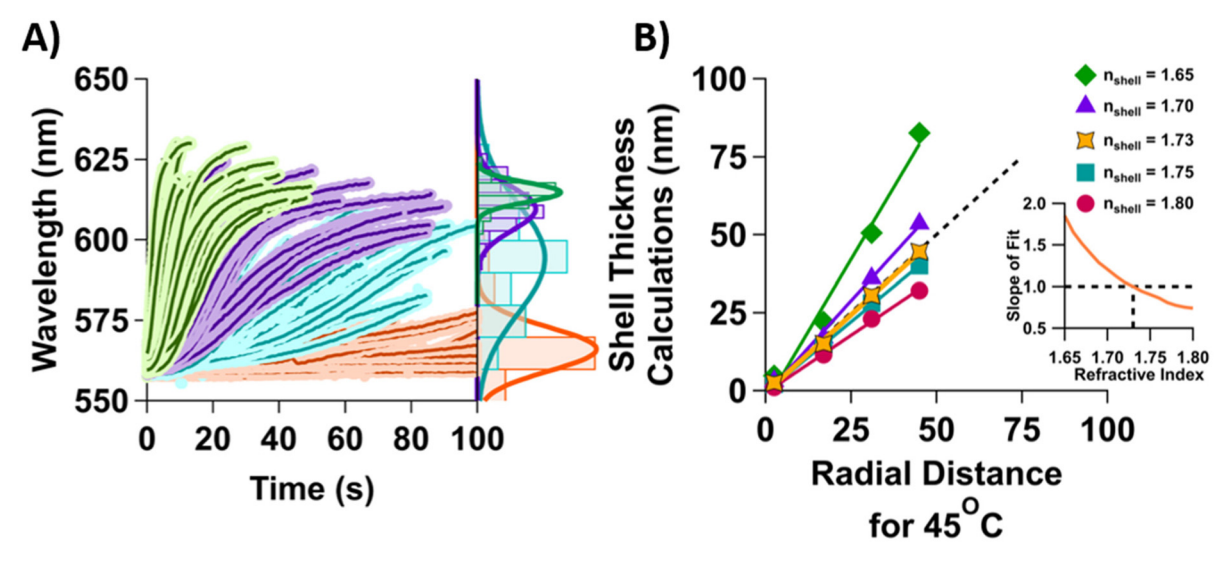


Fig. 6 (A) Left: Testing the growth of 4-TBim on an 80 nm AuNP at different trapping laser powers. 30 mW (orange), 40 mW (blue), 50 mW (purple), and 60 mW (green). Right: Gaussian fits for histogram of the final wavelength achieved during growth illustrating average final wavelengths 30 mW (568 nm), 40 mW (595 nm), 50 mW (611 nm), and 60 mW (622 nm). Histograms are of the last 3% of data from each particle. (B) Plotting the shell thickness predicted from plasmon scattering cross section calculations against the radial distance that the particle is predicted to be above 45 °C. Inset plots the slope of each fit line against its corresponding refractive index to illustrate which refractive index shell agrees best with our expectation. This occurs at $n \approx 1.7$.

This dependence on power suggests that the growth is selflimited by the maximum temperature at the surface of the AuNP. Using heating models for the temperature near a nanoparticle surface, 21,22 we estimate shell thickness in post processing analysis. We and others have shown previously that the surface temperature of the AuNP and the rate of temperature decay into the solution scales with trapping laser power (see ESI Fig. S13†). 21,22 At 30 mW of trapping laser power, the AuNP surface temperature reaches 46.5 °C, decaying to 45 °C within ~3 nm, while at 50 mW the surface reaches 64 °C, decaying to 45 °C within 31 nm. Experimentally, we observe almost no growth at 30 mW, suggesting that ~45 °C is the threshold condition for ZIF growth, which is similar to tempin previously reported encapsulation procedures.^{2,8} As the trapping power is increased, the region around the particle where temperatures exceed 45 °C extends to further radial distances (see Fig. S13†), allowing for thicker ZIF shell growth. We can estimate the thickness of the ZIF shells grown at each power setting by comparing the average measured asymptotic wavelength to our scattering cross section model shown in Fig. 4B. In Fig. 6B, we plot this extrapolated thickness from the model in Fig. 4 against the radial extent of the regions corresponding to $T \ge 45$ °C. The y = x line is indicated in dashes. These results for 4-TBim confirm the growth of high-density crystals with $n \approx 1.7$, which is significantly higher than for ZIF crystals grown in bulk synthesis. Importantly, this is the first report of a ZIF grown from this 4-TBim precursor and our results here indicate that its shell thickness can be finely tuned by surface temperature via laser power modulation.

Conclusion

In this work, we demonstrate a new technique for controllably growing high density ZIF crystals on the surface of a single isolated AuNP and characterize ZIF material properties and growth dynamics using purely optical techniques. We first show that optically trapping an AuNP in the presence of ZIF precursors will result in significant and reproducible changes to the particle plasmon scattering spectra. Our observations imply that a new material is displacing the solvent near the surface of the AuNP. We perform a Raman scattering measurement, in tandem with growth, in the presence of 2-Mim and Zn(NO₃)₂ precursors, and confirm that a ZIF-8 crystal encapsulates the trapped AuNP under these conditions. We then successfully grow crystals using different imidazole derivatives of varying molecular size: 2-Mim, 4-TBim, Bim, and 6-BBim. ZIF shells grown from these compounds follow the expected trend of larger molecule yielding less dense crystals, as confirmed by the relative red shifts of their scattering spectra. In all cases, the grown crystals exhibit a markedly higher refractive index (n \approx 1.7) than in crystals grown using bulk methods, indicating that we achieve higher density ZIFs using our directed single particle heating method. Significantly, the ZIF grown using 4-TBim has not been reported previously. Here, we find that

shell thickness can be reliably controlled by adjusting the incident laser power of the trapped Au NP.

The technique of localized heating for directed ZIF growth developed here raises the prospect of achieving custom designed particle shapes and surface morphologies for applications such as SERS substrate preparation, gas sequestration, and catalytic site design. While the yield in these experiments is limited to a single particle at a time, the fine-tuned control demonstrated here suggests that we could design and build custom nanoscale to mesoscale structures from individual particles as building blocks. We demonstrate controlled growth of distinct materials using four different organic linkers combined with two different metal ion centers in three different solvent environments. These successes suggest that this technique can be expanded to accommodate any MOF for which temperature can drive growth. Further experiments are needed to determine the range of possible substrate materials (gold, silver, aluminum, etc.) and other MOF nanoshells materials.

Author contributions

Daniel Jackson and Maria Kamenetska designed the study, planned the experiments and wrote the manuscript. Daniel Jackson collected and analyzed data. Maitreya Rose assisted in data collection and analysis.

Conflicts of interest

The authors declare no competing financial interests.

References

- 1 G. Zheng, S. De Marchi, V. López-Puente, K. Sentosun, L. Polavarapu, I. Pérez-Juste, E. H. Hill, S. Bals, L. M. Liz-Marzán, I. Pastoriza-Santos and J. Pérez-Juste, Encapsulation of Single Plasmonic Nanoparticles within ZIF-8 and SERS Analysis of the MOF Flexibility, *Small*, 2016, 12(9), 3935–3943, DOI: 10.1002/smll.201600947.
- 2 Q. Q. Chen, R. N. Hou, Y. Z. Zhu, X. T. Wang, H. Zhang, Y. J. Zhang, L. Zhang, Z. Q. Tian and J. F. Li, Au@ZIF-8 Core-Shell Nanoparticles as a SERS Substrate for Volatile Organic Compound Gas Detection, *Anal. Chem.*, 2021, 93(19), 7188–7195, DOI: 10.1021/ACS.ANALCHEM.0C05432/ASSET/IMAGES/LARGE/AC0C05432_0007.JPEG.
- 3 P. Falcaro, F. Carraro, M. D. J. Velásquez-Hernández, E. Astria, W. Liang, L. Twight, C. Parise, M. Ge, Z. Huang, R. Ricco, X. Zou, L. Villanova, C. O. Kappe and C. Doonan, Phase Dependent Encapsulation and Release Profile of ZIF-Based Biocomposites, *Chem. Sci.*, 2020, 11(13), 3397– 3404, DOI: 10.1039/C9SC05433B.
- 4 Y. Li, J. Jin, D. Wang, J. Lv, K. Hou, Y. Liu, C. Chen and Z. Tang, Coordination-Responsive Drug Release inside Gold Nanorod@metal-Organic Framework Core-Shell Nanostructures for near-Infrared-Induced Synergistic

Chemo-Photothermal Therapy, *Nano Res.*, 2018, **11**(6), 3294–3305, DOI: **10.1007/S12274-017-1874-Y**.

Nanoscale

- 5 N. Salehifar, P. Holtmann, A. Prakash Hungund, H. Soleimani Dinani, R. E. Gerald and J. Huang, Calculations of Adsorption-Dependent Refractive Indices of Metal-Organic Frameworks for Gas Sensing Applications, Opt. Express, 2023, 31(5), 7947–7965, DOI: 10.1364/ OE.478427.
- 6 I. U. Khan, M. H. D. Othman, A. Jilani, A. F. Ismail, H. Hashim, J. Jaafar, M. A. Rahman and G. U. Rehman, Economical, Environmental Friendly Synthesis, Characterization for the Production of Zeolitic Imidazolate Framework-8 (ZIF-8) Nanoparticles with Enhanced CO2 Adsorption, *Arabian J. Chem.*, 2018, 11(7), 1072–1083, DOI: 10.1016/J.ARABJC.2018.07.012.
- 7 G. Kumari, K. Jayaramulu, T. K. Maji and C. Narayana, Temperature Induced Structural Transformations and Gas Adsorption in the Zeolitic Imidazolate Framework ZIF-8: A Raman Study, *J. Phys. Chem. A*, 2013, **117**(43), 11006–11012, DOI: **10.1021/jp407792a**.
- 8 L. Chen, Y. Peng, H. Wang, Z. Gu and C. Duan, Synthesis of Au@ZIF-8 Single- or Multi-Core-Shell Structures for Photocatalysis, *Chem. Commun.*, 2014, **50**(63), 8651–8654, DOI: **10.1039/C4CC02818**J.
- 9 S. Wang and X. Wang, Metal-Organic Frameworks Multifunctional Metal-Organic Frameworks for Photocatalysis, *Small*, 2015, **11**(26), 3097–3112, DOI: **10.1002/smll.201500084**.
- 10 G. Fan, X. Zheng, J. Luo, H. Peng, H. Lin, M. Bao, L. Hong and J. Zhou, Rapid Synthesis of Ag/AgCl@ZIF-8 as a Highly Efficient Photocatalyst for Degradation of Acetaminophen under Visible Light, *Chem. Eng. J.*, 2018, 351, 782–790, DOI: 10.1016/J.CEJ.2018.06.119.
- 11 X. Xie, Y. Zhang, L. Zhang, J. Zheng, Y. Huang and H. Fa, Plasmon-Driven Interfacial Catalytic Reactions in Plasmonic MOF Nanoparticles, *Anal. Chem.*, 2023, 93(39), 13219–13225, DOI: 10.1021/acs.analchem.1c02272.
- 12 E. Saeb and K. Asadpour-Zeynali, A Novel ZIF-8@ZIF-67/Au Core-Shell Metal Organic Framework Nanocomposite as a Highly Sensitive Electrochemical Sensor for Nitrite Determination, *Electrochim. Acta*, 2022, 417, 140278, DOI: 10.1016/J.ELECTACTA.2022.140278.
- 13 L. Zhao, G. Niu, F. Gao, K. Lu, Z. Sun, H. Li, M. Stenzel, C. Liu and Y. Jiang, Gold Nanorods (AuNRs) and Zeolitic Imidazolate Framework-8 (ZIF-8) Core—Shell Nanostructure-Based Electrochemical Sensor for Detecting Neurotransmitters, ACS Omega, 2021, 6(48), 33149–33158, DOI: 10.1021/acsomega.1c05529.
- 14 S. Lu, M. Hummel, K. Chen, Y. Zhou, S. Kang and Z. Gu, Synthesis of Au@ZIF-8 Nanocomposites for Enhanced Electrochemical Detection of Dopamine, *Electrochem. Commun.*, 2020, 114, 106715, DOI: 10.1016/J. ELECOM.2020.106715.
- 15 X. Yang, Y. Liu, S. Hei Lam, J. Wang, S. Wen, C. Yam, L. Shao and J. Wang, Site-Selective Deposition of Metal-Organic Frameworks on Gold Nanobipyramids for Surface-

- Enhanced Raman Scattering, *Nano Lett.*, 2021, **21**(19), 8205–8212, DOI: **10.1021/acs.nanolett.1c02649**.
- 16 K. S. Park, Z. Ni, A. P. Cô, J. Y. Choi, R. Huang, F. J. Uribe-Romo, H. K. Chae, M. O'Keeffe and O. M. Yaghi, Exceptional Chemical and Thermal Stability of Zeolitic Imidazolate Frameworks, *Proc. Natl. Acad. Sci. U. S. A.*, 2006, 103(27), 10186–10191, DOI: 10.1073/pnas.0602439103.
- 17 Y. Pan, Y. Liu, G. Zeng, L. Zhao and Z. Lai, Rapid Synthesis of Zeolitic Imidazolate Framework-8 (ZIF-8) Nanocrystals in an Aqueous System, *Chem. Commun.*, 2011, 47, 2071–2073, DOI: 10.1039/c0cc05002d.
- 18 N. Gugin, J. A. Villajos, I. Feldmann and F. Emmerling, Mix and Wait a Relaxed Way for Synthesizing ZIF-8, *RSC Adv.*, 2022, 12, 8940–8944, DOI: 10.1039/d2ra00740a.
- 19 J. Cookney, W. Ogieglo, P. Hrabanek, I. Vankelecom, V. Fila and N. E. Benes, Dynamic Response of Ultrathin Highly Dense ZIF-8 Nanofilms, *Chem. Commun.*, 2014, 50, 11698– 11700, DOI: 10.1039/c4cc04754k.
- 20 F. Casini, G. M. B. Viggiani and S. M. Springman, Breakage of an Artificial Crushable Material under Loading, *Granular Matter*, 2013, 15(5), 661–673, DOI: 10.1007/S10035-013-0432-X/FIGURES/16.
- 21 D. J. Jackson, B. A. Dawes and M. Kamenetska, Simultaneous Force and Darkfield Measurements Reveal Solvent-Dependent Axial Control of Optically Trapped Gold Nanoparticles, *J. Phys. Chem. Lett.*, 2023, **14**(11), 2830–2836, DOI: **10.1021/acs.jpclett.3c00088**.
- 22 Y. Seol, A. E. Carpenter and T. T. Perkins, Gold Nanoparticles: Enhanced Optical Trapping and Sensitivity Coupled with Significant Heating, Opt. Lett., 2006, 31(16), 2429–2431, DOI: 10.1364/OL.31.002429.
- 23 F. Han, T. Armstrong, A. Andres-Arroyo, D. Bennett, A. Soeriyadi, A. A. Chamazketi, P. Bakthavathsalam, R. D. Tilley, J. J. Gooding and P. J. Reece, Optical Tweezers-Based Characterisation of Gold Core-Satellite Plasmonic Nano-Assemblies Incorporating Thermo-Responsive Polymers, *Nanoscale*, 2020, 12, 1680–1687, DOI: 10.1039/c9nr07891f.
- 24 A. Andres-Arroyo, F. Wang, W. J. Toe and P. Reece, Intrinsic Heating in Optically Trapped Au Nanoparticles Measured by Dark-Field Spectroscopy, *Biomed. Opt. Express*, 2015, 6(9), 3646, DOI: 10.1364/boe.6.003646.
- 25 J. Yang, Y. B. Zhang, Q. Liu, C. A. Trickett, E. Gutiérrez-Puebla, M.Á Monge, H. Cong, A. Aldossary, H. Deng and O. M. Yaghi, Principles of Designing Extra-Large Pore Openings and Cages in Zeolitic Imidazolate Frameworks, *J. Am. Chem. Soc.*, 2017, 139(18), 6448-6455, DOI: 10.1021/jacs.7b02272.
- 26 K. Pearce, F. Wang and P. J. Reece, Dark-Field Optical Tweezers for Nanometrology of Metallic Nanoparticles, Opt. Express, 2011, 19(25), 25559–25569, DOI: 10.1557/ mrs2005.100.
- 27 J. W. M. Osterrieth, D. Wright, H. Noh, C. W. Kung, D. Vulpe, A. Li, J. E. Park, R. P. Van Duyne, P. Z. Moghadam, J. J. Baumberg, O. K. Farha and D. Fairen-Jimenez, Core-Shell Gold Nanorod@Zirconium-Based

Paper Nanoscale

- Metal-Organic Framework Composites as in Situ Size-Selective Raman Probes, J. Am. Chem. Soc., 2019, 141(9), 3893-3900, DOI: 10.1021/jacs.8b11300.
- 28 G. Lu, S. Li, Z. Guo, O. K. Farha, B. G. Hauser, X. Qi, Y. Wang, X. Wang, S. Han, X. Liu, J. S. Duchene, H. Zhang, Q. Zhang, X. Chen, J. Ma, S. Chye, J. Loo, W. D. Wei, Y. Yang, J. T. Hupp and F. Huo, Imparting Functionality to a Metal-Organic Framework Material by Controlled Nanoparticle Encapsulation, Nat. Chem., 2012, 4, 310-316, DOI: 10.1038/NCHEM.1272.
- 29 L. Zhao, G. Niu, F. Gao, K. Lu, Z. Sun, H. Li, M. Stenzel, C. Liu and Y. Jiang, Gold Nanorods (AuNRs) and Zeolitic **Imidazolate** Framework-8 (ZIF-8) Core-Shell Nanostructure-Based Electrochemical Sensor for Detecting Neurotransmitters, ACS Omega, 2021, 6(48), 33149-33158, DOI: 10.1021/acsomega.1c05529.
- 30 E. Sani and A. Dell'Oro, Spectral Optical Constants of Ethanol and Isopropanol from Ultraviolet to Far Infrared, 60, 137-141, DOI: 10.1016/j. Opt. Mater., 2016, optmat.2016.06.041.
- 31 U. Hohenester and A. Trügler, MNPBEM A Matlab Toolbox for the Simulation of Plasmonic Nanoparticles, Comput. Phys. Commun., 2012, 183(2), 370-381, DOI: 10.1016/J.CPC.2011.09.009.
- 32 K. M. McPeak, S. V. Jayanti, S. J. P. Kress, S. Meyer, S. Iotti, A. Rossinelli and D. J. Norris, Plasmonic Films Can Easily Be Better: Rules and Recipes, ACS Photonics, 2015, 2(3), 326-333, DOI: 10.1021/ph5004237.

- 33 A. M. Aboraia, A. A. A. Darwish, V. Polyakov, E. Erofeeva, V. Butova, H. Y. Zahran, A. F. A. El-Rehim, H. Algarni, I. S. Yahia and A. V. Soldatov, Structural Characterization and Optical Properties of Zeolitic Imidazolate Frameworks (ZIF-8) for Solid-State Electronics Applications, Opt. Mater., 2020, 100, 109648, DOI: 10.1016/J.OPTMAT.2019.109648.
- 34 M. R. Ryder, Z. Zeng, Y. Sun, I. Flyagina, K. Titov, E. M. Mahdi, T. D. Bennett, B. Civalleri, C. S. Kelley, M. D. Frogley, G. Cinque and J.-C. Tan, Dielectric Properties of Metal-Organic Frameworks Probed via Synchrotron Infrared Reflectivity, ArXiv, 2018, preprint, DOI: 10.48550/arXiv.1802. 06702.
- 35 N. C. Keppler, K. Deli, J. Hindricks and P. Behrens, Large Refractive Index Changes in ZIF-8 Thin Films of Optical Quality, RSC Adv., 2022, 12, 5807-5815, DOI: 10.1039/ d1ra08531j.
- 36 J. Hromadka, B. Tokay, S. James, R. P. Tatam and S. Korposh, Optical Fibre Long Period Grating Gas Sensor Modified with Metal Organic Framework Thin Films, Sens. Actuators, B, 2015, 221, 891-899, DOI: 10.1016/J. SNB.2015.07.027.
- 37 G. Cai, P. Yan, L. Zhang, H.-C. Zhou and H.-L. Jiang, Metal-Organic Framework-Based Hierarchically Porous Materials: Synthesis and Applications, Chem. Rev., 2021, 121, 12278-12326, DOI: 10.1021/acs.chemrev.1c00243.
- 38 Berkeley Global Science Institute. Reticular Chemistry Naming and Numbering Database. https://globalscience.berkeley.edu/database.